Analyst

Accepted Manuscript

ROYAL SOCIETY OF CHEMISTRY

www.rsc.org/analyst

Analyst

RSCPublishing

ARTICLE

Effect of pore diameter in nanoporous anodic alumina optical biosensors

Cite this: DOI: 10.1039/xoxxoooooox

G. Macias, J. Ferré-Borrull, J. Pallarès and L.F. Marsal[a]

Received ooth January 2012,
Accepted ooth January 2012

DOI: 10.1039/xoxxoooooox

www.rsc.org/analyst

The influence of pore diameter over the optical response of nanoporous anodic alumina (NAA) films is analyzed by reflectance interference spectroscopy. NAA manufactured by the two-step anodization procedure in oxalic acid exhibiting three well-defined pore diameter distributions with pores of 32 ± 4, 50 ± 3, and 73 ± 2 nm are studied. The optical detection of biomolecules is investigated by serially dosing protein A, human IgG and anti-human IgG into the nanoporous matrix using a custom-made flow cell. The results demonstrate that the transduction signal, the variation of effective optical thickness upon IgG binding to protein A (ΔEOT), depends of the nanopore diameter: for small pore diameter (32 nm) no significant differences in signal are observed for different protein concentrations whereas for larger pore diameters (50 nm and 73 nm) the signal increases for increasing concentration from 10 to 100 µg•mL-1. Our experiments also show that this signal can be further enhanced by amplification with anti-human IgG due to the multiple binding events between the antigen and antibody. These results will enable the development of more sensitive interferometric biosensors based on NAA.

Introduction

Label-free biomolecular sensors are devices that monitor binding events between two biomolecules in real time. This makes them an interesting research tool for medical, environmental and biochemical sciences. A biosensor consists in a surface loaded with a recognition element that specifically reacts with the analyte. This binding event is then transduced into a quantifiable signal such as an optical[1,2] or an electrochemical response[3,4].

Interferometric biosensors are a specific kind of optical biosensor. They rely on a very sensitive technique called reflectance interference spectroscopy (RIfS). RIfS bases on monitoring the interference pattern resulting from illuminating a thin film with a white light. This pattern depends on the effective optical thickness (EOT) which in turn, depends on the refractive index of the thin film (n) and its thickness (L) (EOT=2nL). The binding of analyte molecules to the sensor surface results in the formation of an organic adlayer. In an initial work, planar RIfS biosensors monitored this binding event by measuring thickness shifts (ΔL) in the reflectance spectrum. To do so, the refractive indexes of the biological adlayer and the thin film had to be similar[2]. Further development of RIfS technology led to the use of porous materials in an attempt to increase the sensitivity of the technique. Porous thin films have a larger surface binding area for analyte capture. However, when RIfS is applied to these materials, it does not measure ΔL but a refractive index shift (Δn).

The first porous interferometric biosensor was based on porous silicon (pSi)[5]. Further development of porous interferometric biosensors continued with pSi as the sensing matrix due to the well-known fabrication techniques available[6-15]. The main disadvantage of such sensors was the instability of pSi at physiological conditions which resulted in a baseline drift due to the dissolution of the porous layer in the aqueous environment[7]. In an attempt to improve the resistance of pSi several approaches been proposed to passivate the surface. The most common technique for pSi passivation is obtaining porous silicon dioxide (pSiO2) by thermal oxidation[16]. This process increases the stability of the porous structure, but still some dissolution of the pSiO2 matrix could be appreciated[17]. Better approaches for enhancing the stability of pSi in aqueous environments are thermal carbonization[17-18] and TiO2 coating[19]. Another approach would be to use nanoporous anodic alumina (NAA) as the porous matrix[20-27]. NAA consists in close-packed, self-ordered parallel pores whose structural characteristics can be easily tuned by adjusting the electrochemical etching conditions and applying pore widening post-treatments[28]. Moreover, NAA has greater stability than pSi at physiological pH[21,29] and its surface can be functionalized in order to covalently attach selective receptors[30-33].

To date, few optimization studies have been carried out in order to determine the optimal structure for biosensing purposes. Pore diameter is one of the most limiting factors[34-37]. When pore diameters are too small, they can hinder protein diffusion inside the structure and when pores are too large, the refractive index

contrast will decrease an also there is the possibility of scattering light and thus, the structure will not be suitable for interferometric sensing. In an initial work, pSi with four different pore diameters were studied using a model enzyme linked immunosorbent assay (ELISA) was used to evaluate antibody binding capacity[34]. This experiment demonstrated the minimum pore diameter necessary to distinguish specific from non-specifc binding. However, even though the effect of pore size could be appreciated, the pore diameter distribution was wide and just one concentration was evaluated. The effect of porosity has been theoretically calculated for the adsorption of bovine serum albumin (BSA) in NAA waveguide sensors[35]. But no experimental proof of this effect was reported. Kumeria et al. reported an optimization study of NAA using RIfS[36]. In this study, different pore diameters with distinct layer thicknesses and metal coatings were evaluated. However, the conclusions over the optimal structure were based on the resulting reflectance spectra and not on an actual sensing experiment. Recently, electrochemical impedance spectroscopy (EIS) was used to determine the influence of pore diameter on impedance nanopore biosensors[37]. This work was able to demonstrate the influence of pore diameter in EIS in the detection of different concentrations of biotin in streptavidin-functionalized NAA. Nevertheless, biotin is a low molecular weight analyte (MW_{biotin} = 244.31 Da << $MW_{human\ IgG}$ = 150-170 kDa) and thus, investigation of the influence of pore diameter in heavier biomolecular analytes such as immunoglobulins is of great interest.

In this work, we present a thorough study the effect of pore diameter over the sensing performance of a NAA monolayer biosensor in order to define the best pore diameter for biosensing purposes. To assess this issue, we prepared three different sets of NAA samples with the same pore length and three different narrow pore diameter distributions. The resulting structure was monitored in real-time using RIfS. The samples were serially infiltrated with protein A, two concentrations of 10 and 100 $\mu g \cdot mL^{-1}$ of human IgG, and anti-human IgG.

Experimental

Materials.

Aluminium (Al) foil (thickness = 250 µm, purity = 99,999%) was purchased from Goodfellow. Oxalic acid ($H_2C_2O_4$), ethanol (C_2H_5OH), acetone ($(CH_3)_2CO$), perchloric acid ($HClO_4$), phosphoric acid (H_3PO_4), chromium trioxide (CrO_3), protein A from staphylococcus aureus (SpA), human IgG from human serum, and anti-human IgG produced in goat were purchased from Sigma Aldrich. Double de-ionized (DI) water (18.6 MΩ, Purelab Option-Q) was used for all the solutions unless otherwise specified.

Fabrication.

Al substrates were first degreased in acetone and further cleaned with ethanol (EtOH), DI water and dried under a stream of air. Prior to anodization, Al substrates were electropolished in a mixture of EtOH and perchloric acid ($HClO_4$) 4:1 (v:v) at 20 V and 5 ºC for 4 min. During the electropolishing procedure, the stirring direction was alternated every 60 s. Then, the electropolished Al substrates were cleaned in DI water, EtOH, DI water and dried under a stream of air. Subsequently, the first anodization step was performed in oxalic acid ($H_2C_2O_4$) 0.3 M at 40 V and 4-6 ºC for 20 h and cleaned with DI water, EtOH, DI water and dried under a stream of air. Then, the grown aluminium oxide was selectively dissolved in a mixture of phosphoric acid (H_3PO_4) 0.4 M and chromic acid (H_2CrO_4) 0.2 M at 70 ºC for 3 h. The resulting patterned Al was cleaned in DI water, EtOH, DI water and dried under a stream of air. Afterwards, a second anodization step was performed under the same conditions until a total charge of 2.08 C was reached. Finally, the pores were widened by wet chemical etching in phosphoric acid (H_3PO_4) 5 % wt. at 35 ºC for 0, 10 and 20 min and the resulting samples cleaned in DI water, EtOH, DI water and dried under a stream of air[28].

Immunosensor experiments.

NAA samples were placed in a flow cell and a baseline with PBS was acquired prior to protein dosing. Subsequently, proteins were serially dosed to the NAA sample in three steps at a constant flow rate of 1 $mL \cdot min^{-1}$. Step I corresponds to protein A (100 $\mu g \cdot mL^{-1}$), step II corresponds to human IgG (10 or 100 $\mu g \cdot mL^{-1}$) and step III corresponds to anti-human IgG (100 $\mu g \cdot mL^{-1}$). Washing steps of 30-40 min in PBS between proteins were performed in order to remove free and loosely bound proteins.

Data acquisition.

Reflectance spectra of the NAA samples in the 500-1000 nm range were obtained using a halogen light and a CCD spectrometer (Avantes). Light was directed to the surface at a normal angle through a fiber optic cable consisting of six illuminating waveguides and one reading waveguide coupled to an optical lens which focused the light on top of the NAA. The light reflected by the NAA sample was collected by the reading waveguide and directed to the CCD spectrometer. Finally, a discrete Fourier transform was applied using the algorithm developed by Sailor[10]. The position of the resulting Fourier transform peak was monitored in real-time in order to detect the binding events among the different proteins and the resulting data was de-noised using an adjacent averaging of 200 data points.

Results and discussion

Structural characterization.

SEM micrographs showed high-density uniform self-ordered pores throughout the samples. Fig. 1a, 1b and 1c show the top-view images of samples corresponding to pore widening times (t_{pw}) of t_{pw} = 0 min, t_{pw} =10 min and t_{pw} = 20 min respectively. The pictures show an increasing pore diameter for increasing

t_{pw} and an almost perfect triangular lattice within the image scale. Fig. 1d shows a cross section of one of the as produced NAA monolayers showing highly parallel straight pores without pore branching and with a pore length (L_p) of L_p = 4.6 ± 0.1 µm. Thanks to these straight nanochannels, interpore diffusion of the proteins is avoided. This picture also shows part of the sample upper surface, with the good triangular arrangement and the different domains.

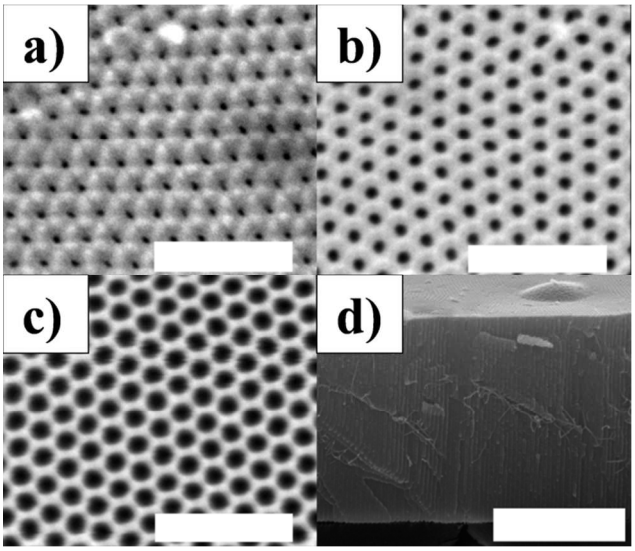

Fig. 1. SEM micrographs of the NAA films used in this study. Top views of (a) t_{pw} = 0 min, (b) t_{pw} = 10 min, and (c) t_{pw} = 20 min (scale bars = 500 nm); (d) cross section of a NAA film (t_{pw} = 0 min) (scale bar = 3 µm).

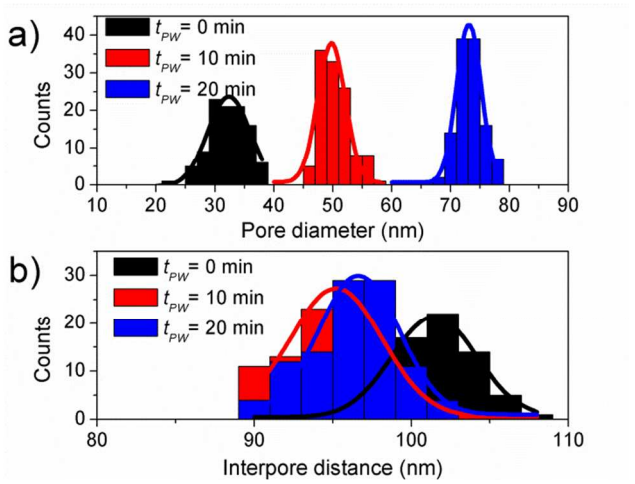

Fig. 2. Histogram of (a) pore diameter distribution (d_p), and (b) interpore distance (D_{int}).

Fig. 2 presents the results of the image analysis of the SEM micrographs. Fig. 2a shows the statistical analysis of pore diameters (d_p) with the number of counts at intervals of width 2 nm. The distribution of the pore sizes can be fitted to a Gaussian where the average pore size and standard deviation can be estimated. The results showed a narrow pore diameter distribution in all samples with d_p= 32 ± 4 nm, d_p= 50 ± 3 nm and d_p= 73 ± 2 nm for the samples with t_{pw} = 0 min., t_{pw} =10 min. and t_{pw} = 20 min. respectively. Fig. 2b shows the results of the statistical analysis of the interpore distance (D_{int}). The results showed again narrow distributions of D_{int}= 102 ± 3 nm, D_{int}= 95 ± 3 nm and D_{int}= 97 ± 3 nm corresponding to the same three pore widening times, respectively. These results demonstrate the monodispersion of the diameters studied and the repeatability of the interpore distance within the 90-105 nm range using our fabrication conditions.

Optical characterization.

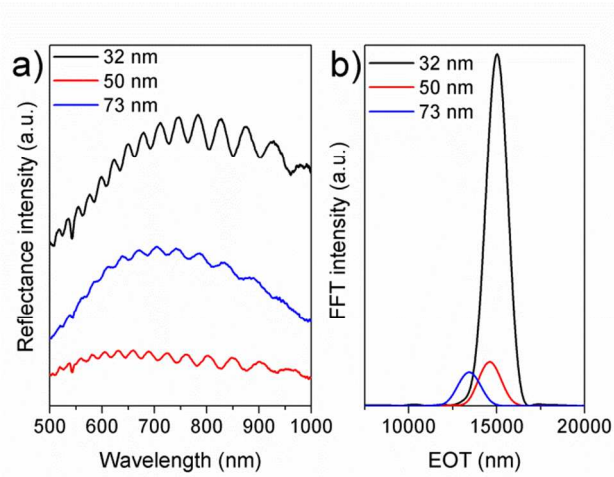

Fig. 3. Optical characterization of the NAA monolayer biosensors. (a) Reflectance spectra of the NAA monolayers, (b) Fourier transform of the reflectance spectra in (a).

Fig. 3 shows the optical characterization of the NAA monolayers before protein infiltration. Fig. 3a shows the reflected intensity spectra of three NAA monolayers in the 500-1000 nm range corresponding to the three t_{pw} considered in this work. The spectra displayed consist in a series of oscillations arising from Fabry-Pérot interference of the light reflected at the top (air/NAA) and bottom (NAA/Al) interfaces. These interferences follow the Fabry-Pérot relationship:

$$m\lambda = 2nL, \quad (1)$$

where m is the order of each oscillation, λ is the wavelength of the corresponding maximum, n is the effective refractive index of the layer and L is its thickness. The right hand part of this equation corresponds to the effective optical thickness (EOT) of the layer. The spectra of these NAA monolayers with average pore diameters of 32, 50 and 70 nm show a total of 15, 14 and 13 oscillations respectively. Furthermore, the amplitude of the intensity oscillations also decreases with increasing porosity. Since all samples have the same thickness, these differences are related with the refractive index of the porous layer (n_{layer}), which in turn depends of the layer porosity (or nanopore diameter). As the pore sizes and interpore distance are smaller than the measurement wavelengths, the refractive index of the layer can be related to porosity with an effective medium approximation[24]:

$$(1-P)\frac{n_{Al_2O_3}^2-n_{layer}^2}{n_{Al_2O_3}^2+2n_{layer}^2}+P\frac{n_{medium}^2-n_{layer}^2}{n_{medium}^2+2n_{layer}^2}=0\,, \qquad (2)$$

where n_{layer} is the effective refractive index of the layer, nmedium is the refractive index of the material filling the pores, n_{Al2O3} is the refractive index of the alumina and P is the porosity of the layer.

Thus, since the wavelength difference between two consecutive maxima depends inversely of n_{layer} (as it can be deduced from eq. 1) the number of oscillations decreases for increasing porosity due to the decrease in optical contrast. Furthermore, the amplitude of the oscillations depends directly of the refractive index difference at the two layer interfaces (n_{Al}-n_{layer}) and (n_{layer}-n_{air}). The reduction of n_{layer} with increasing porosity results in a reduction of the (n_{Air}-n_{layer}) difference while the (n_{Al}-n_{layer}) remains essentially constant because of the high extinction coefficient of the aluminium.

Fig. 3b shows the Fourier transform resulting from applying a Fourier analysis as described in literature[10,25]. The Fourier transform simplifies the analysis of the reflectance spectra by transforming reflectance oscillations into a single peak. The position of the Fourier transform peak (FTP) corresponds to the EOT of the porous layer. Analysis of the position of the FTPs in fig. 3b shows decreasing EOT values as d_p increases. This is in good agreement with the previous analysis of the number of oscillations present in the reflectance spectra. The height of the FTP is related with the amplitude of the interference oscillations. The FTP heights in fig. 3b decrease with increasing d_p, what is also in good agreement with the amplitude of the interferences present in fig. 3a.

Protein infiltration.

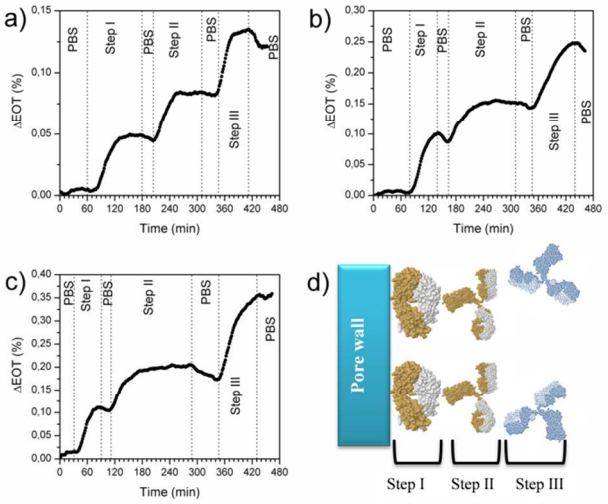

Fig. 4. Real-time ΔEOT for pore diameters of a) 32 ± 4 , b) 50 ± 3 and c) 73 ± 2 nm; d) schematic representation of protein reactions. Step I, II and III corresponds to SpA , human IgG and anti-human IgG dosing respectively.

Fig. 4a, 4b and 4c show the real-time measurement of the EOT shift (ΔEOT) during the inmunosensing experiments described in the experimental section for NAA monolayers with d_p = 32 ± 4 nm, d_p = 50 ± 3 nm and d_p = 73 ± 2 nm, respectively. The first 30-60 min correspond to the first phase in which PBS is dosed and a baseline for the measurement is taken. The next phase corresponds to the dosing of a 100 μg•mL^{-1} protein A solution (SpA) for 60-120 min followed by rinsing with PBS for 30-40 min. SpA adsorbs to the inner pore walls of the NAA monolayers by electrostatic interactions and each SpA molecule acts as a capture probe for two human IgG units[13,21]. The behaviour of the ΔEOT is the same for the three studied dp. Initially, ΔEOT increases rapidly until it reaches saturation. Then, upon rinsing with PBS, ΔEOT decreases slightly as a result of the removal of free and loosely bound SpA molecules. The final ΔEOT (i.e. after the PBS rinse) is bigger for larger d_p of the NAA monolayer.

Subsequently, a 100 μg•mL^{-1} solution of human IgG was flowed for 120-180 min followed by rinsing with PBS for 30-40 min. Human IgG is attached to SpA through its Fc portion with high affinity. Similarly to SpA, the behaviour of the ΔEOT is the same in the three d_p studied. Initially, ΔEOT increases rapidly until it reaches saturation and then, upon rinsing with PBS, ΔEOT decreases slightly as a result of the removal of free and loosely bound human IgG molecules. Again, the final ΔEOT depends on the d_p of the NAA monolayer used, being bigger for larger pores. It is important to stress that the same experiments were performed with a lower concentration of 10 μg•mL^{-1}of human IgG and the same trends were observed: an initial fast increase of the ΔEOT until a saturation is reached followed by a slight decrease in ΔEOT with PBS rinsing (see Electronic Supplementary Information, Figure 1).

Finally, a 100 μg•mL^{-1} solution of anti-human IgG of was flowed for 60 min followed by rinsing with PBS for 30-40 min. Anti-human IgG binds to both light and heavy chains of human IgG. Since each human IgG consists of two heavy chains and two light chains, a single human IgG ensures enough binding sites for 4 anti-human IgG molecules. Thanks to this feature anti-human IgG enables amplification of the optical signal of the previously immobilized human IgG. During this last amplification step the concentration was maintained to 100 μg•mL^{-1} in all experiments. Binding of anti-human IgG proves that human IgG is not denaturalized after binding to SpA and that it is properly oriented for anti-human IgG binding. As in the phases with the two human IgG concentrations and SpA dosing, the behaviour of anti-human IgG binding is the same in the three d_p studied. Initially, ΔEOT increases rapidly until it reaches saturation. Then, upon rinsing with PBS, ΔEOT decreases slightly as a result of the removal of free and loosely bound anti-human IgG molecules. In this case, the final ΔEOT also depends on the d_p of the NAA monolayer used, being bigger for larger pores.

Fig. 5 shows the final ΔEOT after each protein infiltration step (dosing with a molecule until saturation is reached and rinsing with PBS to remove the loosely bound molecules) is shown as a function of the pore diameter d_p. The error bars correspond to

the measurement noise estimated in the first PBS dosing phase (for specific values see Electronic Supplementary Information, Table 2). Step I corresponds to SpA infiltration, step II corresponds to human IgG infiltration and step III corresponds to the signal amplification using anti-human IgG. As it was observed in Fig. 4, ΔEOT in step I increases with increasing d_p. It has to be remarked that this increment is more noticeable between pores of 32 and 50 nm (a variation of 5,6 % in ΔEOT for each nm in diameter) than between pores of 50 and 73 nm (0,8 % in ΔEOT for each nm in diameter). ΔEOT for step II and for the two considered concentrations follows a similar trend as for step I, showing higher ΔEOT as d_p increases. By comparing the ΔEOT between the two concentrations employed in this study (10 and 100 µg•mL-1) a clear difference in behaviour can be observed: pores with d_p = 32 show no difference in ΔEOT for the concentrations studied, whereas pores with d_p = 50 nm and d_p = 73 nm show a bigger ΔEOT for bigger human-IgG concentration with a difference of 0.03 and 0.05 % respectively. The fact that ΔEOT stabilizes at different values for different human IgG concentrations suggests that the amount of IgG bound to SpA is directly related to the concentration of IgG in the PBS, and thus that there exists an equilibrium between dissolved and bound IgG. However, this only happens for the two biggest pore radii, while for d_p = 32 nm no difference can be observed, what could indicate that the binding or the diffusion dynamics of IgG are different for such pore size. Another fact that supports this assumption is that the trend of ΔEOT with d_p in both the case of SpA and of IgG: the value for the d_p = 32 nm pores is smaller than what could be estimated from the values for d_p = 50 nm and d_p = 73 nm and if a linear relationship were assumed. This smaller value can also be an indication of differences in diffusion dynamics of the molecules in the smaller diameter pores.

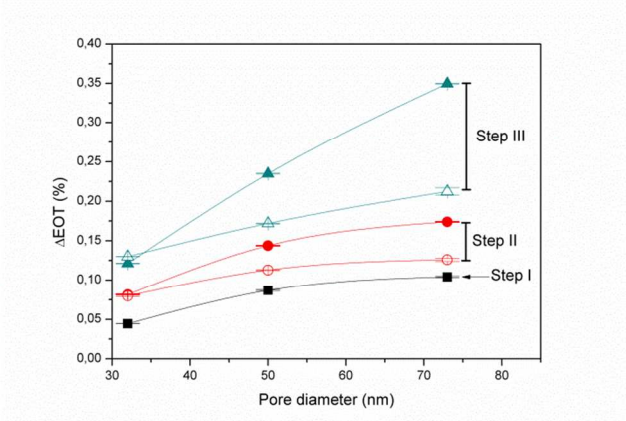

Fig. 5. Resulting ΔEOT after each immobilization step for each dp. Black squares represent SpA dosing, red circles represent human IgG dosing and green triangles represent anti-human IgG dosing. Solid scatter represents for 100 µg•mL^{-1} and void for 10 µg•mL^{-1} of human IgG.

The ΔEOT in step III shows a slightly different trend than for step I and step II. ΔEOT in step III also increases with d_p, but with a bigger increment in ΔEOT with d_p than in steps I and II. This is caused by the amplification effect of the anti-human IgG when attaching to the four possible binding sites in the IgG molecule. On the other hand, after this step III no significant differences can be observed in the ΔEOT for the two studied IgG concentrations for the pores with d_p = 32 nm. Nevertheless, an amplification of the ΔEOT with respect step II is also noticed. Despite the fact that each human IgG has 4 possible binding sites for anti-human IgG, the amplification factors observed are in the range between 1.5 and 2 (see Electronic Supplementary Information, Table 3). All the results presented here indicate that pores with d_p = 73 nm show the best detection performance upon protein dosing.

Conclusions

The influence of the nanoporous anodic alumina pore size on the sensing of human IgG proteins by the RIfS methods was studied. This was accomplished by measuring the changes in effective optical thickness of different NAA films with different pore diameters but with the same thickness upon serial infiltration of SpA, human IgG and anti-human IgG. The results demonstrate that the sensitivity of the ΔEOT depends of the pore diameter of the structure. The sensing procedure consists of three steps: step I is the dosing of protein A (SpA), step II is the actual sensing step and consists of dosing human-IgG in different concentrations, finally, step III is an amplification step consisting of dosing anti-human-IgG at a fixed concentration. If the ΔEOT after one of these steps is compared for different pore diameters, it can be concluded that larger pore diameters lead to higher ΔEOT in all cases.

The NAA films with d_p = 50 nm and d_p = 73 nm showed different ΔEOT after step II for the two considered concentrations of 10 and 100 µg•mL^{-1} of human IgG. During infiltration, our experiments showed that the ΔEOT reached a stable value after a given reaction time, and this value was different for each concentration. This is in good agreement with the expected behaviour of an affinity-based biological reaction. However, NAA films with d_p = 32 nm showed no significant difference between the two concentrations of human IgG, both after step II.

Further dosing of anti-human IgG amplified the optical response of the NAA films maintaining the same noise level. This amplification strategy could help to lower the limit of the detection of NAA-based interferometric biosensors as it improves the signal without increasing the noise level. From our results and based on the noise level obtained, we estimate a limit of detection of 1 µg•mL^{-1} in the third step using NAA with d_p =73 nm.

We believe that the results presented here will enable the development of more sensitive NAA optical biosensors.

Acknowledgements

This work was supported by the Spanish Ministry of Economy and competitiveness (MINECO) under grant number, TEC2012-34397 and by Catalan authority under project AGAUR 2014 SGR 1344. .

Notes and references

[a] Department of Electronic, Electric and Automatics Engineering, Universitat Rovira i Virgili, Avda. Països Catalans 26, 43007 Tarragona, Spain; E-mail: lluis.marsal@urv.cat; Tel: (34) 977 559625Address here.

† Electronic Supplementary Information (ESI) available: Experimental fabrication tables, ΔEOT values after each step, real-time ΔEOT graphs for 10 μg•mL-1 of human IgG and ΔEOT vs concentration graph. See DOI: 10.1039/b000000x/

1 A. Brecht and G. Gauglitz, Optical probes and transducers, *Biosens. & Bioelectron.*, 1995, **10**, 923-936.
2. J. Piehler, A. Brecht, and G. Gauglitz. Affinity detection of low molecular analytes. *Anal. Chem.*, 1995, **68**, 139-143.
3. M. Darder, P. Aranda, M. Hernández-Vélez, E. Manova and E. Ruiz-Hitzky. Encapsulation of enzymes in alumina membranes of controlled pore size, *Thin Sol. Films,* **2006**, 495, 321-326.
4. A. de la Escosura-Muñiz and A. Merkoçi. Label-free voltammetric immunosensor using a nanoporous membrane based platform. *Electrochem. Comm.*, 2010, **12**, 859-863.
5. V. S.-Y. Lin, K. Motesharei, K.-P.S. Dancil, M.J. Sailor, and M.R. Ghadiri. A porous silicon-based optical interferometric biosensor. *Science*, 1997, **278**, 840-843.
6. A. Janshoff, K.-P. S. Dancil, C. Steinem, D.P. Greiner, V.S.-Y. Lin, C. Gurtner, K. Motesharei, M.J. Sailor, and M.R. Ghadiri. Macroporous p-Type Silicon Fabry-Perot Layers. Fabrication, Characterization, and Applications in Biosensing. *J. Am. Chem. Soc.*, 1998, **120**, 12108-12116.
7. K.-P. S Dancil,. D.P. Greiner, and M.J. Sailor, A Porous Silicon Optical Biosensor: Detection of Reversible Binding of IgG to a Protein A-Modified Surface. *J. Am. Chem. Soc.,* 1999, **121**, 7925-7930.
8. L. A. DeLouise and B.L. Miller. Quantitative Assessment of Enzyme Immobilization Capacity in Porous Silicon. *Anal. Chem.*, 2004, **76**, 6915-6920.
9. A. Tinsley-Bown, R.G. Smith, S. Hayward, M.H. Anderson, L. Koker, A. Green, R. Torrens, A.-S. Wilkinson, E.A. Perkins, D.J. Squirrell, S. Nicklin, A. Hutchinson, A.J. Simons and T.I. Cox. Immunoassays in a porous silicon interferometric biosensor combined with sensitive signal processing. *Phys. Stat. Sol. (a),* 2005, **202**, 1347-1356.
10. C. Pacholski, M. Sartor, M.J. Sailor, F. Cunin and G.M. Miskelly. Biosensing Using Porous Silicon Double-Layer Interferometers: Reflective Interferometric Fourier Transform Spectroscopy. *J. Am. Chem. Soc.,* 2005, **127**, 11636-11645.
11. C. Pacholski, C. Yu, G.M. Miskelly, D. Godin and M.J. Sailor. Reflective Interferometric Fourier Transform Spectroscopy: A Self-Compensanting Label-Free Immunosensor Using Double-Layers of Porous SiO2. *J. Am. Chem. Soc.*, 2006, **128**, 4250-4252.
12. C. Pacholski and M.J. Sailor. Sensing with porous silicon double layers: A general approach for background suppression. *Phys. Stat. Sol. (c)*, 2007, **4**, 2088-2092.
13. M.P. Schwartz, S.D. Alvarez and M.J. Sailor. Porous SiO2 Interferometric Biosensor for Quantitative Determination of Protein Interactions: Binding of Protein A to Immunoglobulins Derived from Different Species. *Anal. Chem.,* 2007, **79**, 327-334.
14. M.Y. Chen and M.J. Sailor. Charge-Gated Transport of Proteins in Nanostructured Optical Films of Mesoporous Silica. *Anal. Chem.,* 2011, **83**, 7186-7193.
15. M.Y. Chen, M.D. Klunk, V.M. Diep and M.J. Sailor. Electric-Field-Assisted Protein Transport, Capture and Interferometric Sensing in Carbonized Porous Silicon Films. *Adv. Mater.,* 2011, **23**, 4537-4542.
16. M. Hecini, A. Khelifa, B. Bouzid, N. Drouiche, S. Aoudj and H. Hamitouche. Study of formation, stabilization and properties of porous silicon and porous silica. *J. Phys. Chem. Solids*, 2013, **74**, 1227-1234.
17. T. Jalkanen, V. Torres-Costa, E. Mäkilä, M. Kaasalainen, R. Koda, T. Sakka, Y.H. Ogata, and J. Salonen. Selective Optical Response of Hydrolytically Stable Stratified Si Rugate Mirrors to Liquid Infiltration. *ACS Appl. Mater. Interfaces*, 2014, **6**, 2884-2892.
18. N. Naderi, M.R. Hashim, J. Rouhi, and H. Mahmodi. Enhanced optical and electrical stability of thermally carbonized porous silicon. *Mater. Sci. Semicond. Process.*, 2013, **16**, 542-546.
19. J. Li and M.J. Sailor. Synthesis and characterization of a stable, label-free optical biosensor from TiO2-coated porous silicon. *Biosens. Bioelectron.*, 2014, **55**, 372-378.
20. S. Pan and L.J. Rothberg. Interferometric Sensing of Biomolecular Binding Using Nanoporous Aluminum Oxide Templates. *Nano Lett.,* 2003, **3**, 811-814.
21. S.D. Alvarez, C.-P. Li, C.E. Chiang, I.K. Schuller, and M.J. Sailor.. A label-free porous alumina interferometric immunosensor. *ACSNano*, 2009, **3**, 3301-3307.
22. A. Santos, V.S. Balderrama, M. Alba, P. Formentín, J. Ferré-Borrull, J. Pallarès and L.F. Marsal. Tunable Fabry-Pérot interferometer based on nanoporous anodic alumina for optical biosensing purposes. *Nanoscale Res. Lett.,* 2012, **7**, 370-4.
23. A. Santos, G. Macias, J. Ferré-Borrull, J. Pallarès and L.F. Marsal. Photoluminescent Enzymatic Sensor Based on Nanoporous Anodic Alumina. *ACS Appl. Mater. Interfaces*, 2012, **4**, 3584-3588.
24. A. Santos, V.S. Balderrama, M. Alba, P. Formentín, J. Ferré-Borrull, J. Pallarès and L.F. Marsal. Nanoporous Anodic Alumina Barcodes: Toward Smart Optical Biosensors. *Adv. Mater.,* 2012, **24**, 1050-1054.
25. G. Macias, L.P. Hernández-Eguía, J. Ferré-Borrull, J. Pallarès and L.F. Marsal. Gold-Coated Ordered Nanoporous Anodic Alumina Bilayers for Future Label-Free Interferometric Biosensors. *ACS Appl. Mater. Interfaces*, 2013, **5**, 8093-8098.
26. T. Kumeria, A. Santos and D. Losic. Ultrasensitive Nanoporous Interferometric Sensor for Label-Free Detection of Gold(III) Ions. *ACS Appl. Mater. Interfaces*, 2013, **5**, 11783-11790.
27. T. Kumeria, M.M. Rahman, A. Santos, J. Ferré-Borrull, L.F. Marsal and D. Losic. Structural and Optical Nanoengineering of Nanoporous Anodic Alumina Rugate Filters for Real-Time and Label-Free Biosensing Applications. *Anal. Chem.,* 2014, **86**, 1837-1844.
28. M.M. Rahman, E. Garcia-Caurel, A. Santos, L.F. Marsal, J. Pallarès and J. Ferré-Borrull. Effect of the anodization voltaje on the pore-widening rate of nanoporous anodic alumina. *Nanoscale Res. Lett.,* 2012, **7**, 474-7.
29. T. Van Gestel, C. Vandecasteele, A. Nuekenhoudt, C. Dotremont, J. Luyten, R. Leysen, B. Van der Bruggen and G. Maes. Alumina and titania multilayer membranes for nanofiltration: preparation, characterization and chemical stability. *J. Membr. Sci.,* 2002, **207,** 73-89.
30. A. M. M. Jani, I.M. Kempson, D. Losic and N.H. Voelcker. Dressing in Layers : Layering Surface functionalities in Nanoporous

Aluminum Oxide Membranes. *Angew. Chem. Int. Ed.,* 2012, **49**, 7933-7937.

31. J. ter Maat, R. Regeling, C.J. Ingham, C.A.G.M: Wijers, M. Giesbers, W.M. de Vos and H. Zuilhof. Organic Modification and Subsequent Biofuntionalization of Porous Anodic Alumina Using Terminal Alkynes. *Langmuir*, 2011, **27**, 13606-13617.
32. L. Treccani, T.Y. Klein, F. Meder, K. Pardun and K. Rezwan, K. Functionalized ceramics for biomedical, biotechnological and environmental applications. *Acta Biomater.,* 2013, **9**, 7118-7150.
33. A. Debrassi, A. Ribbera, W.M. de Vos, T. Wennekesand H. Zuilhof Stability of (Bio)Functionalized Porous Aluminum Oxide. *Langmuir,* 2014, **30**, 1311-1320.
34. A.M. Tinsley-Bown, L.T. Canham, M. Hollings, M.H. Anderson, C.L. Reeves, T.I. Cox, S. Nicklin, D.J. Squirrell, E. Perkins, A. Hutchinson, M.J. Sailor and A. Wun. Tuning the Pore Size and Surface Chemistry of Porous Silicon for Immunoassays. *Phys. Stat. Sol. (a)*, 2000, **182**, 547-553.
35. K. Hotta, A. Yamaguchi and N. Teramae. Properties of A Metal Clad Waveguide Sensor Based on A Nanoporous-Metal-Oxide/Metal Multilayer Film. *Anal. Chem.,* 2010, **82**, 6066-6073.
36. T. Kumeria and D. Losic. Controlling interferometric properties of nanoporous anodic aluminium oxide. *Nanoscale Res. Lett.,* 2012, **7**, 88-10.
37. K. Kant, J. Yu, C. Priest, J.G. Shapter and D. Losic. Impedance nanopore biosensor: influence of pore dimensions on biosensing performance. *Analyst*, 2014, **139**, 1134-1140.

This study demonstrates how it is possible to tune the sensitivity of nanoporous anodic alumina optical biosensors by adjusting pore diameter.